A method for accurate and precise pulse arrival time estimation: A case study on high-energy particle detectors

Maynor Giovanni Ballina, Maria Liz Crespo, Sergio Carrato, Romina Soledad Molina, Werner Florian Samayoa, Giovanni Ramponi, Andres Cicuttin

***Abstract*—Advancements in modern electronics have enabled the sampling of signals with higher resolution, facilitating the application of new techniques for the determination of pulse arrival times at detectors. In this paper, we introduce a method for accurate and precise pulse arrival time estimation. This method is immune to offset and slow background variations as well as pulse pile-up effects, requiring a single parameter. The validation is performed through simulations and systematic comparisons with traditional methods, using synthetic pulses and experimental data collected from a particle physics detector. The presented results demonstrated superior accuracy and precision of the proposed method compared to widely used constant fraction discrimination and leading-edge discrimination methods. Moreover, this method is suitable for hardware implementation and can be applied to a wide range of pulse types across various experimental contexts, making it a versatile tool for arrival time estimation in diverse applications.**

***Index Terms*—Features extraction, Digital signal processing, Time of arrival estimation, Linear approximation, Digital filters.**

I. Introduction

In the physical world, numerous phenomena exhibit impulsiveness, characterized by sudden or abrupt appearances followed by rapid evolution in time and subsequent gradual fading. Among typical impulsive phenomena, we can mention high-energy particle detection, radioactive decays, earthquakes, dielectric breakdowns, explosions, avalanches, and nuclear reactions. Transduction of the primary physical quantities associated with these phenomena can generate electrical pulses, which can be amplified, filtered, and digitized using specialized electronic instrumentation. Subsequently, it is often necessary to process the corresponding digital signals to extract meaningful information, facilitating comprehension or control of the underlying phenomena.

In many cases, the primary characteristics associated with a pulse are its amplitude and arrival time. To obtain accurate and precise information about these features, it is crucial to consider the main factors that commonly affect measurements, including noise, irregular background, and pulse pile-up effects.

Specifically, in particle physics, accurate estimation of the arrival time of events poses several challenges, including the need for effective detection under various experimental conditions [1]. Nonetheless, this capability plays a crucial role in numerous experiments and applications, contributing significantly to particle identification, event reconstruction, coordination of particle collisions, data recording, and the understanding of particle interactions [2]. High-quality measurement of the arrival time of particles facilitates the determination of their trajectories, energies, velocities, and other essential parameters, thus aiding in understanding the underlying processes and validating physical theories [3], [4], [5]. In high-energy physics experiments, accurate measurement of the arrival time is indispensable to correctly identify and reconstruct the resultant particles, offering crucial insights into the underlying interaction dynamics and subatomic-scale matter structure [6], [7].

Due to the importance of estimating pulse arrival timing, several methods were proposed in the literature, such as constant fraction discrimination, threshold crossing, leading-edge discrimination, and waveform fitting. Digital Leading-Edge Discrimination (DLED) and Digital Constant Fraction Discrimination (DCFD) are extensively utilized due to their easiness to implement and high temporal resolution in many applications. Aykac et al. [8] provide a detailed comparison of these methods, highlighting their strengths and weaknesses. For instance, DLED boasts simplicity in implementation, prompt response, potential robustness against noise with appropriate threshold selection, and low computational cost. However, it is vulnerable to baseline fluctuations and nonlinear responses to pulses of different amplitudes, diminishing its precision. DCFD is less susceptible to noise and amplitude variations and offers higher precision. Nevertheless, it is more complex to implement than the DLED, requiring parameter adjustments for different pulse variations and consuming more computational resources. In summary, although DLED is simpler and quicker to implement, it may be more sensitive to

This paragraph of the first footnote will contain the date on which you submitted your paper for review.

This work was partially supported by the ICTP TRIL program.

Maynor Giovanni Ballina, Maria Liz Crespo, Romina Soledad Molina, Werner Florian Samayoa, Andres Cicuttin are with Multidisciplinary Laboratory (MLab), STI Unit, The Abdus Salam International Centre for Theoretical Physics (ICTP), Strada Costiera, 11, Trieste, 34151, TS, Italy (e-mail: mballina@ictp.it, mcrespo@ictp.it, rmolina@ictp.it, wflorian@ictp.it, cicuttin@ictp.it).

Maynor Giovanni Ballina, Sergio Carrato, Romina Soledad Molina, Giovanni Ramponi are with the Dipartimento di Ingegneria e Architettura (DIA), Università degli Studi di Trieste (UNITS), Piazzale Europa, 1, Trieste, 34127, TS, Italy (e-mail: maynorgiovanni.ballinaescobar@phd.units.it, carrato@units.it, rominasoledad.molida@phd.units.it, ramponi@units.it).

Maynor Giovanni Ballina is with the IFIM, Escuela de Ciencias Físicas y Matemáticas, Universidad de San Carlos de Guatemala(USAC), Ciudad Universitaria, Zona 12, Guatemala (e-mail: maynor.ballina@ecfm.usac.edu.gt).

noise and threshold selection. DCFD, instead, tends to be more precise and not reliant on a threshold but may be more complex and resource-intensive.

The need to improve arrival time resolution and achieve a more accurate approximation of this measure is evidenced by various studies. Fan et al. [9] introduce a method that consists of the combination of two techniques: DCFD and filter-based interpolation. The utilization of both techniques enables better control over temporal resolution. Jokhovets et al. [10] propose a method using a non-linear approximation of the rising edge of pulses to compute the arrival time.

In this paper, we propose a new method for accurate and precise estimation of the arrival time of a detected pulse using two linear approximations centered around an initial approximation of the pulse onset. Numerical simulations were conducted using two types of synthetic pulses (ramp and semi-Gaussian) to assess the accuracy and precision of the method. In the context of this article, accuracy refers to the closeness of the estimated pulse arrival times to the true values, while precision indicates the consistency or repeatability of these estimations across multiple trials. For further validation, a comparison was made with DCFD and DLED using semi-Gaussian pulses and experimental data collected from a single channel of the ECAL2 calorimeter in the COMPASS experiment at CERN [11], [12], [13].

The main contributions of this article are summarized as follows:

- Mathematical description of a new method for accurate and precise pulse arrival time estimation that requires a single parameter.
- Suitable numerical techniques for possible hardware implementation.
- Statistical analysis on synthetic and experimental data, for a comprehensive comparison of the advantage and disadvantages of our proposed method, DCFD and DLED.

The remainder of this paper is organized as follows: Section II describes the proposed method for arrival time estimation. Section III details the adopted methodology for testing and validation of the method. Results and discussion are presented in Section IV and the conclusions are drawn in Section V.

II. Double Linear Interpolation Method for Pulse Arrival Time Estimation

The method we propose, termed the Double Linear Interpolation Method (DLIM), is designed to estimate the arrival time of a pulse in the presence of noise, irregular backgrounds, or pulse pile-up conditions.

The main idea of the method is qualitatively illustrated in Figure 1, showing a data segment around the onset of a pulse, highlighting the point of maximum concavity (n_0), assumed to be near the true pulse arrival time. Five samples preceding n_0 (red circles) are linearly approximated by the red line, while the subsequent five samples (green circles) are linearly approximated by the green line. The angle θ between these lines quantifies the concavity of the data within these ten samples. The point n_0 corresponds to the minimum θ value obtained within any ten consecutive samples in the analyzed segment, indicating the highest concavity. The method estimates the true pulse arrival time at the intersection of the two linear approximations, occurring at t_0, a time interval q from n_0.

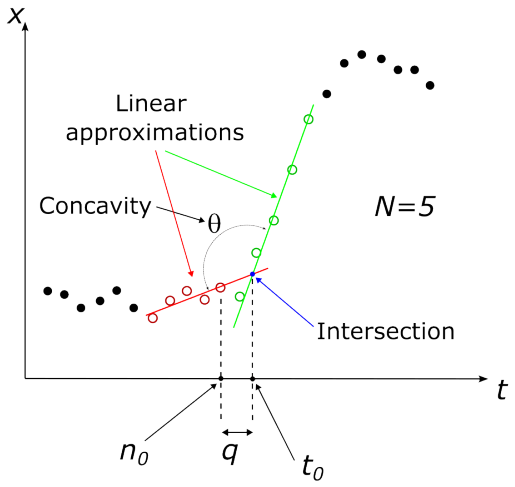

Fig. 1. Double linear interpolation around the point of maximum concavity (n_0) within the analyzed data segment near the onset of a pulse. The five red data samples leading up to n_0 are linearly approximated by the red segment, while the subsequent five green samples are interpolated by the green segment. The estimated pulse arrival time, t_0, is determined at the intersection of these two linear approximations, occurring at a time interval q from n_0.

Operating on digital signals, the method consists of two main steps:

1) First, a coarse estimation of the arrival time with sampling period precision is performed using peak detection over an average second derivative of the signal.
2) Then, a fine estimate is obtained by finding the intersection of the linear interpolations of two consecutive N-sample data segments around the coarse arrival time.

In the following subsections, we present the key considerations for the pulse onset detection strategy and provide the corresponding mathematical explanations of the relevant terms, including the averaged discrete derivatives used in the method to estimate the true pulse arrival time. The number of samples N used in the linear interpolations is the only free parameter of the method.

A. Pulse detection and first coarse arrival time estimation

It is commonly observed that pulse signals exhibit the highest concavity around the time of pulse arrival. Given that the second derivative is an effective measure of local concavity, our initial step involves finding the time at which the second derivative reaches its maximum within a predefined data segment, indicating the likely presence of a pulse for analysis. Subsequently, within the same time window, we locate the maximum second derivative and the corresponding maximum concavity at position n_0 as the initial guess (coarse approximation) for the pulse arrival time.

Using the second derivative, we ensure that the results are not affected by possible signal offsets or constant slope baseline variations. This is because additive terms and constant derivatives are canceled out by second differentiation.

Considering that a critical aspect of the second discrete derivative $\{x_i''\}$ in digital signals $\{x_i\}$ is the amplification of uncorrelated high-frequency noise, we propose averaging the second derivative over the most recent $2N$ samples.

B. Average discrete first and second derivatives

The discrete derivative approximates a function's derivative, representing the rate of change between two consecutive samples. The discrete derivative x'_n of a continuous signal $x(t)$ is defined as follows:

$$x'_n = x_n - x_{n\text{-}1} \tag{1}$$

where, x'_n denotes the discrete derivative computed from the last two consecutive samples of x, which are $x_n = x(t_n)$ and $x_{n\text{-}1} = x(t_{n\text{-}1})$, with t_n and $t_{n\text{-}1}$ representing sampling times expressed as multiples of the sample period t_s.

With this definition, it can be observed that any uncorrelated additive noise in the samples is immediately propagated to the derivative. In the case of uncorrelated white Gaussian noise with a standard deviation of σ_n, the corresponding noise in the discrete derivative has a standard deviation of $\sqrt{2}\,\sigma_n$, which corresponds to an amplification of the sample noise by a factor of $\sqrt{2}$.

To reduce the impact of high-frequency noise, we define an average derivative computed from the last N samples following the approach described in [14] and [15] as follows:

$$\widetilde{x'}_n = \sum_{i=0}^{N-1} d_i\, x_{n\text{-}i} \tag{2}$$

where, $\widetilde{x'}_n$ denotes the averaged first derivative at time index n, $x_{n\text{-}i}$ represents the input signal delayed by i sampling periods, and $\{d_i\}$ are constant coefficients defined as follows:

$$d_i = 1 - \frac{2i}{N-1}, \quad i \in [0, N-1] \tag{3}$$

The convolution expressed in Eq. 2 approximates the discrete derivative, with the exception of a constant scale factor, using the last N samples. This effectively reduces the impact of uncorrelated noise. For instance, using six samples ($N = 6$) to estimate the first derivative using Eq. 2, yields a gain in the output signal-to-noise ratio of about 3.71 times compared to a simple computation with just two samples. For a detailed explanation of this factor and a brief description of the idealizations employed, please refer to Appendix A.

Similarly to Eq. 1, we can define an average second discrete derivative as the difference between the averaged first derivatives evaluated at time indexes n and $n-N$, as follows:

$$\widetilde{x''}_n = \widetilde{x'}_n - \widetilde{x'}_{n\text{-}N} \tag{4}$$

and using Eq. 2 we obtain

$$\widetilde{x''}_n = \sum_{i=0}^{N-1} d_i\, x_{n\text{-}i} - \sum_{i=N}^{2N-1} d_i\, x_{n\text{-}i} \tag{5}$$

where the two sums correspond to the average first derivatives evaluated over segments $\{x_i\}$ with $i \in [0, N-1]$ and $i \in [N, 2N-1]$.

Eq. 5 shows that the coefficients initially defined for an average first derivative can also be used to define an average second derivative. In this case, the coefficients corresponding to $i \in [0, N-1]$ mirror those of $i \in [N, 2N-1]$. This yields the formulation of a new set of coefficients $\{c_i\}$, with $i \in [0, 2N-1]$, to compute an average second derivative in the window of the last $2N$ samples. Notably, this set consistently comprises an even number of coefficients. Fig. 2 illustrates an example with twelve coefficients, where the last six coefficients (blue) mirror the first six (red).

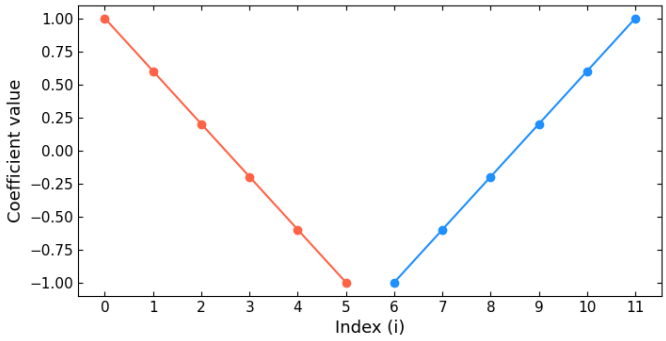

Fig. 2. Coefficients for computing the average second derivative from twelve data samples.

The coefficients $\{c_i\}$ are defined as follows:

$$c_i = \begin{cases} 1 - \frac{2i}{N-1}, & i < N \\ -1 + \frac{2(i-N)}{N-1}, & i \geq N \end{cases} \tag{6}$$

Hence, the average second derivative is determined by the convolution between the coefficients $\{c_i\}$ and the signal $\{x_j\}$, and can be continuously computed using a Finite Impulse Response (FIR) filter.

$$\widetilde{x''_n} = \sum_{i=0}^{2N-1} c_i\, x_{n\text{-}i} \tag{7}$$

As usual, the second derivative provides a measure of concavity, which we leverage to identify the onset of the pulse, where we anticipate the signal's maximum concavity.

We define n_0 as the time index at which the signal presents its maximal concavity in such a way that the average second derivative $\widetilde{x''_i}$ reaches its maximum value at $i = n_0 + N$ within the data segment under analysis. Expressed in units of the sampling period t_s, n_0 serves as our initial (coarse) approximation to the pulse arrival time.

The arrival time of the pulse lies around n_0, and we will estimate it by calculating an additive correction q such that

$$t_0 = n_0 + q \tag{8}$$

where t_0 is our estimation of the true arrival time.

We calculate the value q as the position, relative to n_0, of the intersection of two straight lines that linearly approximate N data samples before and N data samples after n_0.

The value n_0 serves as a pivotal reference for dividing the signal into two sections, $\mathbf{s_1}$ and $\mathbf{s_2}$, consisting of N

consecutive samples $\{x_i\}$, where i ranges from $n_0 - N + 1$ to n_0 for $\mathbf{s_1}$ and from $n_0 + 1$ to $n_0 + N$ for $\mathbf{s_2}$.

DLIM is qualitatively illustrated in Fig. 3 for two overlapping pulses, highlighting areas of maximum concavity. The method computes the average second derivative, where n_0 occurs N samples before the local maximum. Linear approximations are then applied to locate the intersection points corresponding to t_0. Furthermore, it is observed that the method remains effective even as the second pulse arrives while the first one is decaying, showcasing its resilience to data offsets, slow baseline variations, and pulse pile-up scenarios.

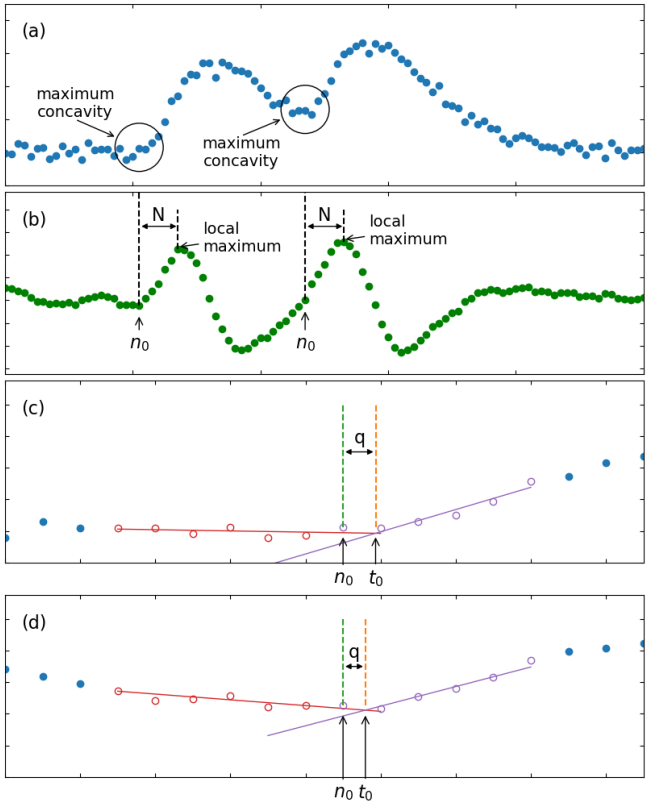

Fig. 3. Qualitative illustration of DLIM applied to two overlapping pulses: (a) Input signal x_i with pileup and maximum concavity region, (b) Average second derivative highlighting the point of maximum concavity n_0, (c) Zoomed-in view of x_i with linear approximations and intersection time t_0 for the first pulse, and (d) Zoomed-in view of x_i with linear approximations and intersection time t_0 for the overlapping pulse.

C. Linear approximations and intersection point

We can approximate the two N-point data segments expressed as the following vectors:

$$\vec{s_1} = \{x_i \,|\, i \in [n_0 - N + 1, n_0]\}$$
$$\vec{s_2} = \{x_i \,|\, i \in [n_0 + 1, n_0 + N]\} \tag{9}$$

by the corresponding linear functions of time referred to n_0:

$$x_i = a_1\,(i - n_0) + b_1 \quad \text{with} \quad i \in [n_0 - N + 1, n_0]$$
$$x_i = a_2\,(i - n_0) + b_2 \quad \text{with} \quad i \in [n_0 + 1, n_0 + N] \tag{10}$$

Here, b_1 and b_2 represent the y-intercepts of the two linear functions, whereas a_1 and a_2 represent their respective angular coefficients.

The coefficients a_1 and a_2 are determined using the least mean squares (LMS) method and can be calculated by taking the scalar product of the vectors $\vec{s_1}$ and $\vec{s_2}$ with a vector $\vec{c_a}$, as follows:

$$a_1 = \vec{s_1} \cdot \vec{c_a}$$
$$a_2 = \vec{s_2} \cdot \vec{c_a} \tag{11}$$

where the vector elements $(\vec{c_a})_i$ are specified as:

$$(\vec{c_a})_i = 6\,\frac{N + 1 - 2\,i}{N - N^3} \tag{12}$$

with $i = 1 \ldots N$.

Similarly, the coefficients b_1 and b_2 can be calculated by taking the scalar product of the vectors $\vec{s_1}$ and $\vec{s_2}$ with vectors $\vec{c_{b1}}$ and $\vec{c_{b2}}$ respectively, as follows:

$$b_1 = \vec{s_1} \cdot \vec{c_{b1}}$$
$$b_2 = \vec{s_2} \cdot \vec{c_{b2}} \tag{13}$$

where the vector elements $(\vec{c_{b1}})_i$ and $(\vec{c_{b2}})_i$ are specified as:

$$(\vec{c_{b1}})_i = -\frac{2N + 2 - 6\,i}{N^2 + N}$$
$$(\vec{c_{b2}})_i = \frac{4N + 2 - 6\,i}{N^2 - N} \tag{14}$$

with $i = 1 \ldots N$.

The interception time q of the two linear approximations is determined by the following expression:

$$q = \frac{b_2 - b_1}{a_1 - a_2} \tag{15}$$

Since the instant of time q of the intersection point is referred to n_0, the arrival time t_0 is simply computed by Eq. 8.

It can be seen that the number of samples N is the sole parameter of the proposed method. This parameter must be empirically optimized according to different concrete aspects such as pulse shape, signal-to-noise ratio, and the probabilistic distribution of the time between consecutive pulses.

The Algorithm 1 describes an implementation of the DLIM method with parameter N operating on the input signal $\{x_i\}$.

Most algorithmic computations rely on linear combinations of input data samples with precalculated coefficients, which makes the method suitable for efficient hardware implementations using FIR filters, as described in Appendix B.

III. Methodology for Validation

The testing and validation of DLIM are separated into method assessment using simulated data and method comparison with DLED and DCFD using both simulated and experimental data. Although the experimental pulses are intrinsically

Algorithm 1 Arrival time estimation using DLIM

Require: N, $\{x_i\}$
Ensure: t_0

$\{c_i\} \leftarrow get\_coefficients\_c_i(N)$
$\widetilde{x''} \leftarrow convolution(\{x_i\}, \{c_i\})$
$n_0 \leftarrow where(earliest(max(\widetilde{x''}))) - N$
$section_1 \leftarrow \{x_i \,|\, i \in [n_0 - N + 1, n_0]\}$
$section_2 \leftarrow \{x_i \,|\, i \in [n_0 + 1, n_0 + N]\}$
$\vec{c_a} \leftarrow get\_coefficients\_a(N)$
$\vec{c_{b1}} \leftarrow get\_coefficients\_b_1(N)$
$\vec{c_{b2}} \leftarrow get\_coefficients\_b_2(N)$
$a_1 \leftarrow dot(section_1, \vec{c_a})$
$b_1 \leftarrow dot(section_1, \vec{c_{b1}})$
$a_2 \leftarrow dot(section_2, \vec{c_a})$
$b_2 \leftarrow dot(section_2, \vec{c_{b2}})$
$q \leftarrow \frac{b_2 - b_1}{a_1 - a_2}$
$t_0 \leftarrow n_0 + q$

precious, the simulation of pulses allows us to freely explore different pulse shapes, amplitudes, and noise. Moreover, the arrival time of the simulated pulses is well known, and it is necessary to correctly estimate the accuracy of the methods.

In several parts of this and the following sections, we use the symbol W to denote the time window size on which the method operates at every time, that is, $W = 2N$.

A. Simulated and experimental datasets

The simulated dataset consists of a total of 100,000 data segments, of which half contains a ramp pulse and half contains a semi-Gaussian pulse. Each data segment is 300 samples long, comprising a pulse plus random noise. To simulate conditions similar to those encountered in detected pulses and the adjustments introduced by analog electronics, we introduce a configurable baseline denoted B (offset) and an additive white Gaussian noise contribution denoted as $\nu(t)$.

To simulate the ramp pulse, the signal $f(t)$ maintains the constant B until the pulse arrival time $t = t_0$. Afterwards, it displays linear behavior with a constant slew rate $S = \Delta A/t_s$, where t_s is the sample period and ΔA is the corresponding increase in amplitude. Thus, a ramp pulse is simply modeled as follows:

$$f(t) = \begin{cases} B + \nu(t), & t < t_0 \\ B + S\,(t - t_0) + \nu(t), & t \geq t_0 \end{cases} \tag{16}$$

Therefore, when setting a constant and known t_0, the dataset consists of simulated pulses in which S varies from 0.01 to 57.54 (a.u.), and the standard deviation σ_n of the Gaussian noise added to the signal varies from 0 to 2 (a.u.). Fig. 4(a) shows a noiseless representation of these pulses.

We use a modified version of the semi-Gaussian pulse that better models the onset. In addition, the mathematical expression of the model is redefined to independently control the pulse amplitude and pulse shape using the parameters α and τ (exponential time constant), respectively, facilitating an independent analysis of both aspects (see Appendix C for more details). The modified semi-Gaussian pulse model is described as follows:

$$f(t) = \begin{cases} B + \nu(t), & t < t_0 \\ B + \alpha e^{-2\frac{t-t_0}{\tau}} \frac{D(t-t_0)}{F} + \nu(t), & t \geq t_0 \end{cases} \tag{17}$$

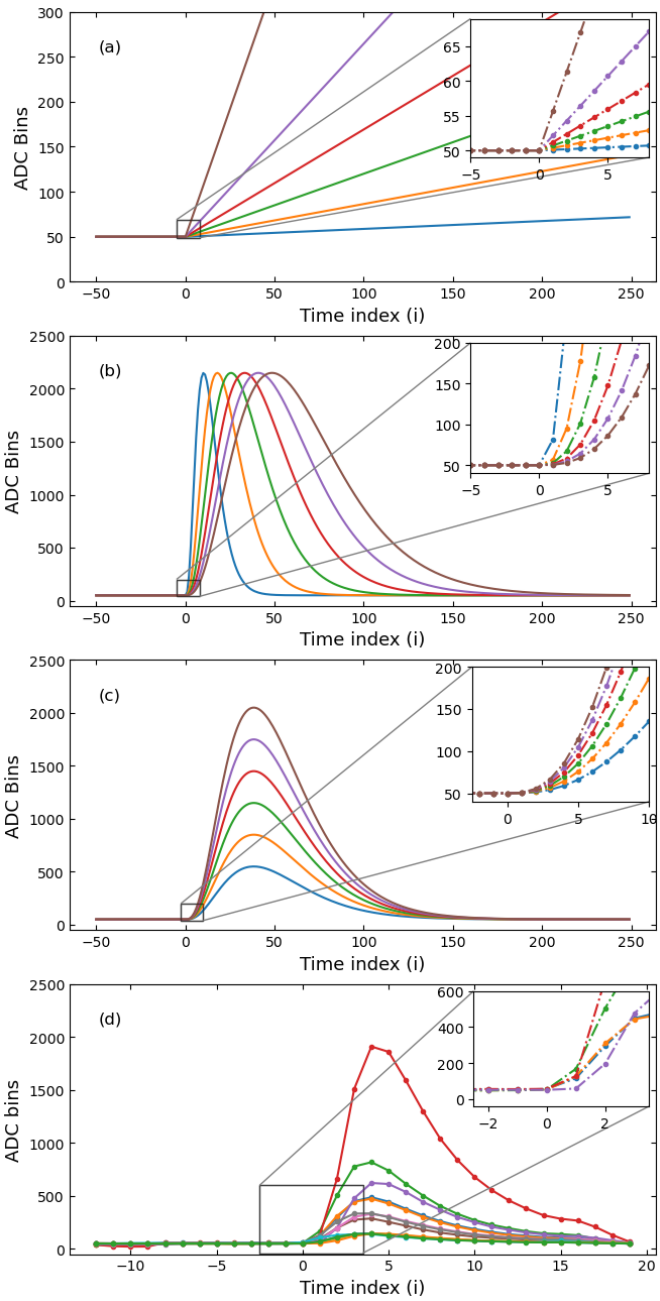

Fig. 4. Different types of pulses: a) Ramp, b) Semi-Gaussian with various exponential times τ, c) Semi-Gaussian with various amplitudes α, and d) Experimental.

where t_0 is the arrival time of the pulse, and $D(t)$ and F are defined by:

$$D(t) = -2\tau^2 e^{\frac{t_0}{\tau}} + e^{\frac{t}{\tau}}(t^2 + 2\tau^2 - 2t\tau)$$

$$F = \frac{-2\tau^2 + e^{\frac{2C}{\tau}}(2\tau^2 - 4\tau C + 4C^2)}{e^{\frac{4C}{\tau}}}$$

and

$$C = \tau + \tau\ \mathrm{ProductLog}(1/e)$$

where $\mathrm{ProductLog}(1/e)$ gives the principal solution for ω in equation $1/e = \omega e^{\omega}$, and is ≈ 0.27846456.

A noiseless representation of these pulses is shown in Fig. 4(b) and 4(c). Fig. 4(b) illustrates pulses with constant amplitude and varying exponential times, while Fig. 4(c) depicts pulses with constant exponential time and varying amplitudes.

In our simulations, the values of the variable pulse parameters were chosen as follows: pulse amplitude (α) between 100 and 2,000 (a.u.), Signal-to-Noise Ratio (SNR) from 10 to 500, and exponential time constant (τ) ranging from 2 to 20 (sampling periods).

Finally, the experimental dataset was acquired using a 12-bit ADC at 80 MSPS and stored in individual 32-sample data segments. Owing to the presence of pulses affected by various acquisition issues (e.g. saturation, pile-up, or time misalignment), preprocessing was conducted on the dataset. This involved selecting analyzable pulses and aligning them according to their maximum amplitudes, as depicted in Fig. 4(d). The experimental dataset consists of 75,600 pulses.

The onset details in Fig. 4, where most of the arrival time information is concentrated, exhibit a similar monotonous growth that is nearly independent of the overall shape of the pulses.

B. Method assessment

To evaluate the DLIM, various numerical simulations were performed under different conditions. The main goal of this study is to specifically analyze the impact of the window size W on the precision and accuracy of the approximated pulse arrival time. We statistically estimate the accuracy of the method as the mean value of the absolute errors obtained from multiple measurements with different realizations of noise, whereas the precision is estimated using the associated standard deviation of these measurements.

The initial simulations use ramp pulses to examine the accuracy and precision of pulse arrival time estimations while varying W from 4 (minimum allowable value of DLIM) to determine appropriate values of W for subsequent studies.

The impact of pulse arrival at different times within the sample period is evaluated, considering that the sampling phase is usually uncontrollable. Various pulse arrival instances are simulated within a sample period using an appropriate value of W. Accuracy and precision are statistically estimated by applying DLIM to a large number of ramp pulses with different realizations of noise and true pulse arrival times uniformly distributed within the sample period.

The next step involves applying DLIM to the ramp pulse dataset to assess how the accuracy and precision depend on the slew rate (S) and noise standard deviation (σ_n).

Similar studies are conducted using DLIM with varying values of W on semi-Gaussian pulses characterized by different parameters τ, α, and σ_n.

C. Method comparison: evaluating DLIM against DLED and DCFD

To provide insights into the relative effectiveness of the proposed method, DLIM is compared with two well-established methods in digital pulse processing: DLED and DCFD, both implemented with linear interpolation. The comparison is done using simulated and experimental semi-Gaussian pulses.

For a fair comparison, we use the same dataset and compare the arrival time (t_0) obtained by the three methods. According to Knoll [16], Aykac et al. [8] and, Zhang et al. [17], the parameters for each method are as follows:

- DLED operates based on the probability distribution of noise modeled as a Gaussian distribution. In this context, the reliability of pulse detection is influenced by the standard deviation (σ_n) of noise. To establish a valid detection, we set a threshold at three times the noise standard deviation above the baseline. This approach ensures that the detected signals are significantly above the expected noise range.
- DCFD involves two configuration parameters that depend on the amplitude of the pulse and its rising time. Since the value of τ and α will vary for these simulations, the fraction is set at 0.4, and the delay is set at the value of the exponential time constant (τ).
- DLIM relies solely on W, which is set at $W = 4\lceil\tau\rceil$. where $\lceil\cdot\rceil$ is the ceiling function.

Because the true value of the pulse arrival time is not available for the experimental data, we have validated the accuracy of the method using a new dataset generated from the simulation of the experimental dataset with the following parameters: α between 100 and 2,500 (a.u.), SNR from 70 to 300, τ of 2.4 (sampling periods), and B ranging from 44 to 56 (a.u.). The parameters used for each method are described below:

- DLED: the threshold is established at three times the noise standard deviation above the baseline.
- DCFD: the fraction is set at 0.4, and the delay is set at two sample times.
- DLIM: W values defined as 4, 6, 8, and 10.

IV. Results and Discussion

The results of the validation process for DLIM are described and compared against DLED and DCFD methods, aiming to provide a thorough understanding of the performance, strengths, and limitations of the proposed method. All presented results on accuracy and precision are expressed in units of sampling period.

A. Ramp pulse time of arrival measurement

Because the second stage of DLIM depends on the linear approximation of two adjacent data segments, the ramp pulse serves to provide a simple pulse model where the linear approximation of the second segment always holds valid independently of the applied window size. Thus, it is possible to easily describe the impact of noise and slew rate across a wide range of window sizes.

The effect of increasing W, as shown in Fig. 5, denotes that higher values of W result in better pulse arrival time estimations. We selected $W = 40$ for the rest of the analysis. In the worst-case scenario of the minimum window size $W = 4$, the linear approximations are based on two points, making the results more susceptible to noise.

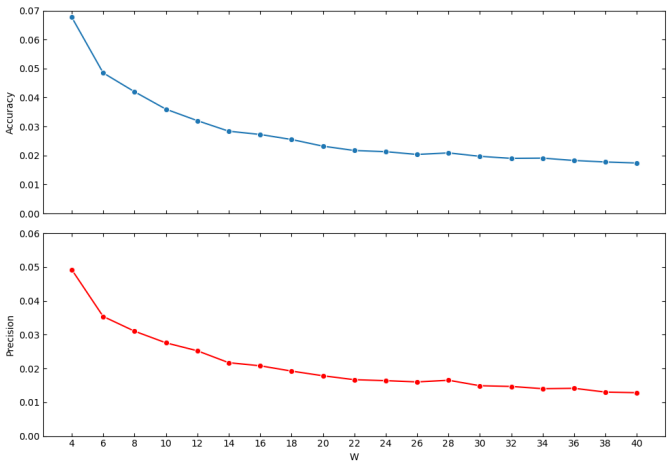

Fig. 5. Improvement in accuracy and precision as W increases, with $S = 60$ and $\sigma_n = 2$.

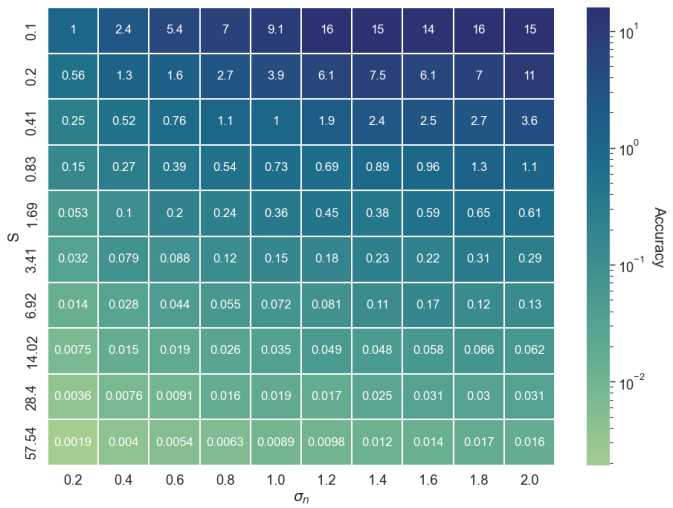

Fig. 6. Influence of slew rate S and noise standard deviation σ_n on DLIM accuracy for $W = 40$.

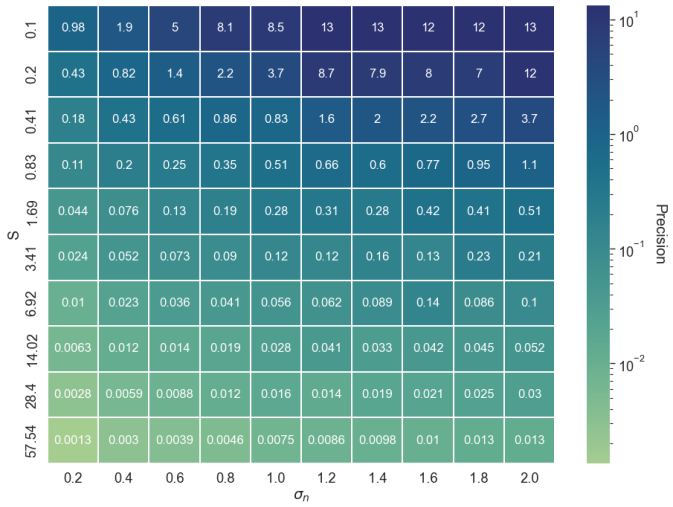

Fig. 7. Influence of slew rate S and noise standard deviation σ_n on DLIM precision for $W = 40$.

Since the sampling times are, in general, asynchronous to the analog impulsive signal, we may assume a uniform random position of the pulse between consecutive samples. Table I shows the variations in accuracy and precision obtained with ten equidistant positions within a sampling period to assess the influence of the true pulse arrival time between consecutive samples, as mentioned in Subsection III-B. The diminished accuracy becomes evident as the pulse arrival time approaches the midpoint between samples. Nevertheless, the variation in accuracy is well below the associated precision, showing that the method is practically insensitive to this aspect.

TABLE I
DLIM ACCURACY AND PRECISION FOR VARIOUS RELATIVE SUB-SAMPLE POSITIONS (IN STEPS OF 0.1 SAMPLE PERIODS) OF THE TRUE PULSE ARRIVAL TIME FOR A RAMP PULSE WITH $S = 60$, $W = 40$, AND $\sigma_n = 0.1$.

relative inter-sample position	accuracy	precision
0.0	0.0094	0.0114
0.1	0.0095	0.0141
0.2	0.0096	0.0128
0.3	0.0098	0.0117
0.4	0.0101	0.0115
0.5	0.0110	0.0114
0.6	0.0094	0.0114
0.7	0.0093	0.0113
0.8	0.0091	0.0109
0.9	0.0091	0.0110

The influence of S and σ_n on accuracy is depicted in Fig. 6, showing a noticeable improvement in accuracy for higher S and smaller σ_n. The impact on precision is illustrated in Fig. 7, which also reflects similar observations.

Special attention must be given on very low values of S, as they lead to closer values of the angular coefficients a_1 and a_2. This results in a small denominator in Eq. 15, consequently increasing susceptibility to noise and potential numerical instabilities.

B. Semi-Gaussian pulse time of arrival measurement

Similarly to the previous study, we start by searching for an optimal value of W based on the exponential time constant τ. Considering the insights from the ramp pulse results, it is clear that larger window sizes provide better resilience to noise.

The plots in Fig. 8 and 9 show the influence of W on the accuracy and precision of the method. In Fig. 8, for $\tau = 2$, it can be observed that the best accuracy is achieved with $W = 10$, while in Fig. 9, for $\tau = 6$, the best accuracy is achieved with $W = 36$. It is also noticeable that the best precision is achieved with $W = 8$ in Fig. 8, while in Fig. 9 the best precision is obtained with values of W between 12 and 24. Both plots present an initial improvement for lower values of W mainly owing to noise attenuation. However, beyond the optimal values of W, the error propagation is progressively amplified due to the decreasing denominator in Eq. 15.

Utilizing $W = 4\lceil\tau\rceil$, we study how τ and SNR influence

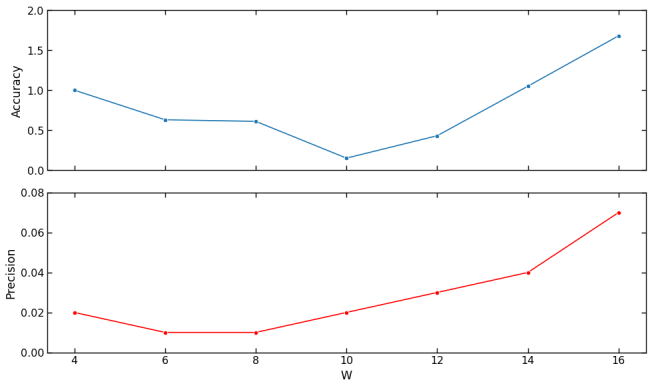

Fig. 8. Variation in DLIM accuracy and precision: with $\tau = 2$ for an even increase of $W \in [4, 16]$ and $SNR = 500$

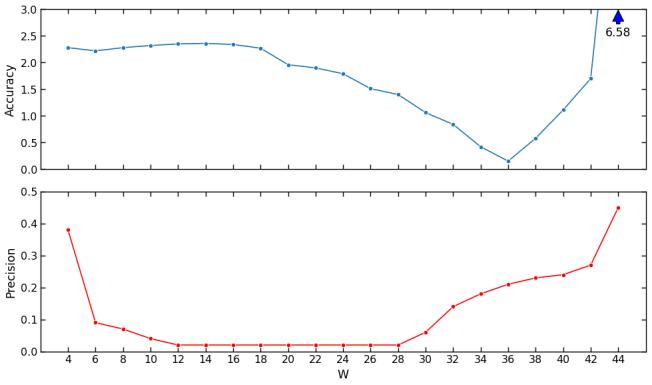

Fig. 9. Variation in DLIM accuracy and precision: with $\tau = 6$ for an even increase of $W \in [4, 40]$ and $SNR = 500$.

accuracy and precision.

The influence of τ and SNR on accuracy and precision are respectably depicted on Fig. 10 and Fig. 11, showing a noticeable improvement for higher SNR and smaller τ. Higher τ values imply lower slew rates, akin to what we observe in the ramp approximation. As expected it shows that the best results are obtained with lower τ values and minimal noise.

Based on the results presented, it is evident that the optimal value for the parameter W in DLIM is primarily determined by the noise and pulse shape. The advantage of having a single parameter simplifies the optimization process of the method.

C. Comparative Evaluation: DLIM Versus DLED and DCFD Methods

This section provides a comparison of the arrival times obtained using DLIM, DCFD and DLED. It showcases the method's applicability through a practical simulation example, followed by an analysis of the experimental dataset.

The comparison between DLIM and DLED, as shown in Table II, indicates that the DLIM consistently achieves higher precision across all variations. In contrast, the accuracy of DLIM fluctuates slightly around a specific value correlated with τ. Although the measurement of t_0 does not demonstrate a higher accuracy, it is consistent with a systematic error

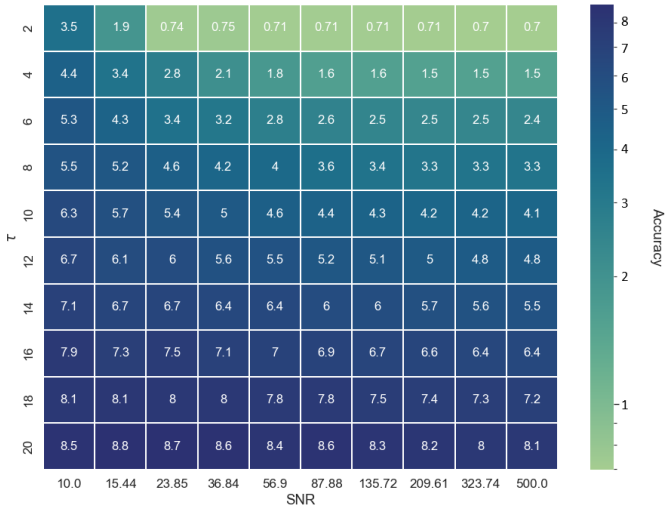

Fig. 10. Influence of τ and SNR on DLIM accuracy with $W = 4\tau$.

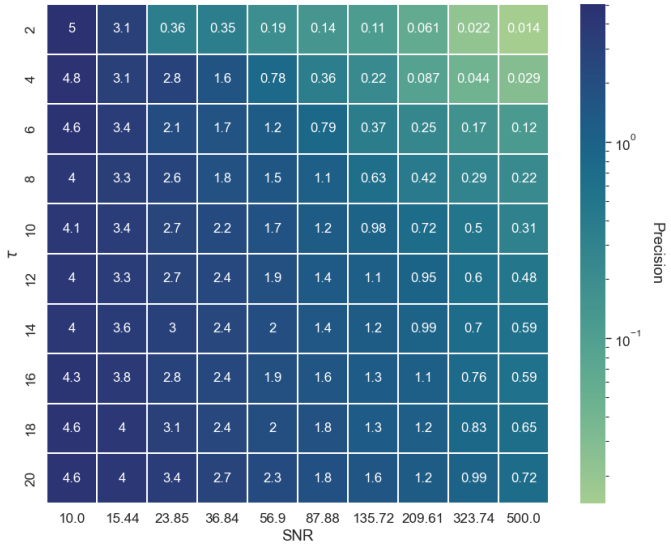

Fig. 11. Influence of τ and SNR on DLIM precision with $W = 4\tau$.

depending on τ and is nearly independent of α and SNR. Consequently, this systematic error can be subtracted from the final value, leading to improved effective accuracy.

The difference between DCFD and DLIM, as shown in Table II, highlights the impact of τ on accuracy and precision. At low τ values, DLIM notably improves the accuracy, albeit with slightly lower precision than DCFD. Noise variation has a minimal effect on DLIM accuracy. However, as τ increases, systematic errors emerge in the accuracy of both the DLIM and DCFD. Nevertheless, the proposed method demonstrates superior accuracy for almost all examined cases. Increasing τ from 2 to 12 leads to a significant worsening of the DCFD precision compared to DLIM, which remains below one sampling period in most presented cases. At low SNR levels, as observed in this case with an SNR of 5, precision begins to deteriorate significantly. However, the accuracy remains relatively consistent across all the presented combinations. Furthermore, the results show an improvement

TABLE II
COMPARISON OF METHODS: DLIM VS DLED VS DCFD FOR SEMI-GAUSSIAN PULSES

Parameters			DLIM		DLED		DCFD	
τ	α	SNR	acc†	precision	acc†	precision	acc†	precision
2	200	200	0.61	0.03	0.05	0.05	2.23	0.03
2	200	50	0.61	0.11	0.31	0.31	2.23	0.08
2	200	5	6.52	11.59	7.95	14.08	23.99	48.26
2	2000	200	0.61	0.03	0.93	4.24	2.23	0.06
2	2000	50	0.61	0.11	1.22	4.85	2.23	0.08
2	2000	5	6.56	11.80	8.06	14.21	24.53	48.57
12	200	200	3.53	0.08	1.28	4.40	4.40	4.34
12	200	50	3.47	0.28	2.01	5.11	5.84	5.10
12	200	5	6.54	3.60	13.84	17.78	7.90	12.74
12	2000	200	3.53	0.08	2.11	5.42	6.87	5.36
12	2000	50	3.47	0.28	2.42	5.76	7.64	5.42
12	2000	5	6.65	3.65	14.14	17.73	8.38	15.65

†Accuracy.

in both precision and accuracy compared to DCFD and DLED.

Based on these results, DLIM emerges as a promising method for measuring the arrival time of semi-Gaussian pulses due to its higher precision and consistent accuracy. However, selecting the optimal parameter W will depend on the specific application and the characteristics of the pulses.

Regarding the experimental dataset, we first simulate the pulses to replicate their average exponential time constant. This simulation accounts for the type of electronics, noise level, baseline, and amplitude range. A dataset is generated that serves as the ground truth by setting the true arrival time at $t = 0$. In the first column of Fig. 12, it is evident that the DCFD and DLIM methods present a nearly Gaussian distribution. Notably, the DLED method faces challenges in accurately determining t_0 values. This issue arises because, unlike the previously analyzed dataset, this contains pulses with varying amplitudes and unstable baseline. For this experiment, we performed DLIM simulations using $W = 4$, 6, 8, and 10.

The second column of Fig. 12 illustrates the histogram comparison of the different methods applied to the experimental dataset. It's evident that the DLED method occasionally shows anticipated estimations of the pulse arrival time. In contrast, both DCFD and DLIM exhibit similar behavior, with DLIM displaying a bell-shaped, narrower distribution.

The experimental results in Table III show that the DLIM method, across a range of W values, significantly outperforms both DLED and DCFD in accuracy and precision for this case study.

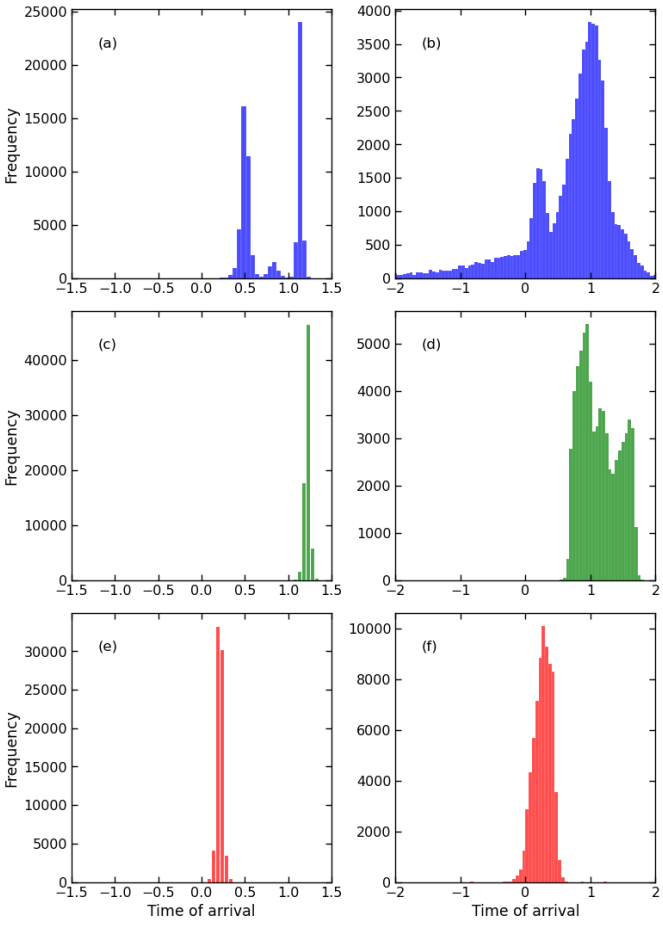

Fig. 12. Histograms of estimated arrival times, expressed in sample periods, for methods DLED (top), DCFD (middle), and DLIM (bottom) applied to simulated (left) and experimental (right) pulses.

TABLE III
METHOD COMPARISON WITH SIMULATED AND EXPERIMENTAL PULSES.

Dataset	Method	Mean†	Precision
Simulated	DLED	0.74	0.61
	DCFD	1.22	0.03
	DLIM4	0.63	0.04
	DLIM6	0.56	0.03
	DLIM8	0.21	0.04
	DLIM10	-0.37	0.01
Experimental	DLED	0.42	1.54
	DCFD	1.14	0.31
	DLIM4	0.86	0.39
	DLIM6	0.70	0.27
	DLIM8	0.26	0.16
	DLIM10	-0.33	0.14

†For simulated pulses this corresponds to the accuracy.

V. CONCLUSION

The proposed method estimates the arrival time of different types of pulses with greater precision than the sampling period of the digital signal. By continuously evaluating an average second discrete derivative, it is possible to measure the concavity of the input signal, detect an incoming pulse, and make a coarse estimation of the arrival time. By linearly approximating two adjacent data segments around the onset of the pulse, the method offers a straightforward, optimal estimation of the pulse arrival time.

With a single parameter, the method can be easily tuned to work effectively for different conditions, including noise, background variations, and pulse pile-up. As is common in most cases, the optimal parameter value must be determined

statistically by evaluating the absolute and relative errors in the estimated pulse arrival times using representative data sets.

The numerical simulations and statistical analysis presented of synthetic and real data have demonstrated the applicability of the method, showing favorable comparisons with widely used methods based on constant fraction discrimination and leading-edge discrimination. The presented analysis and optimization methodology can be easily applied to different types of pulses to assess the method's suitability for each particular case.

Since most algorithmic computations rely on linear combinations of input data samples with precalculated constant coefficients, the method is suitable for efficient hardware implementations using FIR filters. This enables real-time operation with low latency and high performance.

VI. Acknowledgments

We gratefully acknowledge the COMPASS collaboration for providing the experimental data used in this study.

VII. Appendix A: Signal-to-noise ratio improvement in proposed average discrete derivative

We aim to quantify the enhancement in the signal-to-noise ratio resulting from the implementation of the proposed average derivative and investigate how this enhancement depends on the number of samples used. Our analysis will focus solely on the impact of uncorrelated noise, while disregarding other factors such as deviations from linear approximation or noise correlation.

Recalling the definition of average discrete derivative:

$$\widetilde{x'}_n = \sum_{i=0}^{N-1} d_i \, x_{n\text{-}i} \tag{18}$$

To compute the error propagation of the noisy samples $\{x_{n\text{-}i}\}$ to the derivative $\widetilde{x'}_n$ assuming linear approximation, we follow the standard procedure:

$$\delta\widetilde{x'}_n = \sum_{i=0}^{N-1} \frac{\partial(d_i \, x_{n\text{-}i})}{\partial x_{n\text{-}i}} \delta x_{n\text{-}i} \tag{19}$$

Here, $\delta\widetilde{x'}_n$ and $\delta x_{n\text{-}i}$ represent small increments of $\widetilde{x'}_n$ and $x_{n\text{-}i}$ respectively. Given that d_i are constants and $\{\delta x_{n\text{-}i}\}$ correspond to uncorrelated random noise, being independent and identically distributed stochastic variables equal to δx, we add their noise contribution in quadrature as follows:

$$\delta\widetilde{x'}_n = \sqrt{\sum_{i=0}^{N-1} d_i^2} \, \delta x \tag{20}$$

In the latter Equation, we observe the amplification of the noise in the signal x in its average derivative $\widetilde{x'}$. This noise amplification factor (NAF) depends solely on the number of samples, N, used to compute the average derivative, which is:

$$NAF(N) = \sqrt{\sum_{i=0}^{N-1} d_i^2} \tag{21}$$

With the coefficients d_i given in Eq. 3, we can express NAF in closed form

$$NAF(N) = \frac{N(1+N)}{3(-1+N)} \tag{22}$$

Now, let's calculate the corresponding signal amplification in $\widetilde{x'}_n$ relative to the simple first discrete derivative x'_n expressed in Eq. 1. Assuming that the noiseless signal has the same derivative across all N samples, we can rewrite Eq. 18 as follows:

$$\begin{aligned}\widetilde{x'}_n = d_0 \, x_n + d_1 \, x_{n\text{-}1} + d_2 \, x_{n\text{-}2} + \cdots \\ \cdots + d_{N\text{-}2} \, x_{n\text{-}N} + d_{N\text{-}1} \, x_{n\text{-}N+1}\end{aligned} \tag{23}$$

Exploiting the symmetry of the coefficients d_i, that is $d_i = -d_{N-1-i}$, the terms can be rearranged as follows:

$$\begin{aligned}\widetilde{x'}_n = d_0 \, (x_{n\text{-}N+1} - x_0) + d_1 \, (x_{n\text{-}N} - x_1) + \\ + d_2 \, (x_{n\text{-}N\text{-}1} - x_2) + \cdots\end{aligned} \tag{24}$$

Noticing that due to the assumed constant derivative over the N samples region, we have the following relation:

$$x_{n-N-j+1} - x_j = (2j+1)(x_n - x_{n\text{-}1}) = (2j+1)x'_n \tag{25}$$

and we can then express the Eq. 23 as follows:

$$\widetilde{x'}_n = \left(\sum_{i=0}^{N/2} (2i+1) \, d_{N/2-i} \right) x'_n \tag{26}$$

Here, the expression inside parenthesis represents the signal amplification factor (SAF) of $\widetilde{x'}_n$ with respect to x'_n. This factor depends solely on the number of samples, N, used to compute the average derivative, and is defined as follows:

$$SAF(N) = \sum_{i=0}^{N/2} (2i+1) \, d_{N/2-i} \tag{27}$$

Substituting the coefficients $\{d_{N/2-i}\}$ by its definition given in Eq. 3 and simplifying, we have:

$$SAF(N) = \sum_{i=0}^{N/2} (2i+1) \, (1 - \frac{N-2i}{N-1})) \tag{28}$$

This expression can be represented in the following closed form:

$$SAF(N) = \frac{(2+N)(-3+N+N^2)}{6(-1+N)} \tag{29}$$

To assess the improvement factor f in the signal-to-noise ratio of an average derivative, we calculate the ratio between the signal and noise amplification factors, SAF and NAF, respectively, as follows:

$$f(N) = \frac{SAF(N)}{NAF(N)} \tag{30}$$

Substituting the expressions given in Eqs. 22 and 29 and simplifying, we finally obtain:

$$f(N) = \frac{(2+N)(-3+N+N^2)}{2N(1+N)} \tag{31}$$

Table IV presents approximate values of the improvement in signal-to-noise ratio $f(N)$ for different numbers of samples

N used to evaluate the proposed discrete average derivative. Let us recall that these values were computed assuming uncorrelated noise and a constant derivative in the signal across the N samples considered. Any departure from these assumptions will introduce a corresponding error.

TABLE IV
APPROXIMATE VALUES OF THE SIGNAL-TO-NOISE RATIO IMPROVEMENT $f(N)$ FOR SEVERAL VALUES OF N.

N	$f(N)$
2	1.00
4	2.25
6	3.71
8	4.79
10	5.83
12	6.87
14	7.89
16	8.90
18	9.91
20	10.92

The study presented in this appendix is a particular case of differentiation by integration, a subject that has been formally investigated in various articles such as those by Diekema et al. [14] and Liu et al. [15].

VIII. APPENDIX B: ABOUT A POSSIBLE HARDWARE IMPLEMENTATION

Figure 13 illustrates a schematic diagram of a potential hardware implementation of the proposed method. The input signal is directly fed into the FIR filters FIR-a_2 and FIR-b_2 to generate the coefficients a_2 and b_2, respectively. Simultaneously, a delayed version of the input signal, going through the n-tap shift register (denoted as "n-tap SR"), is sent to the FIR filters FIR-a_1 and FIR-b_1 to generate the coefficients a_1 and b_1, respectively. The two subtractors then compute the differences $a_2 - a_1$ and $b_1 - b_2$, which are used as the denominator and numerator, respectively, for the division operation that produces the additive term q. Optimal implementations of hardware dividers can be obtained following the techniques described in Application Specific Arithmetic [18]. To save hardware resources, this implementation reuses the difference $a_2 - a_1$, denoted by $\widetilde{\widetilde{x''_n}}$, as a proportional estimation of the average second discrete derivative $\widetilde{x''_n}$ defined in Equation 7. The proportionality between both definitions of the second derivative is expressed by $\widetilde{x''_n} = \frac{1}{6}N(1-N)\,\widetilde{\widetilde{x''_n}}$, and they present their maximum at the same time index n_0.

A finite state machine labeled "max" detects the earliest maximum value of $\widetilde{x''_n}$ within the present time window and produces n_0, to generate the correct value of t_0, which is given by the sum of n_0 and q. The state machine generates n_0 taking into account the latency of the divider and the time window for checking the maximum of $\widetilde{\widetilde{x''_n}}$.

The proposed method is well-suited for implementation in Digital Pulse Processors, where pulse detection and feature extraction are performed in separate functional blocks. While the maximum of the averaged second derivative can be used to detect pulse arrival via a discriminative threshold, the method does not inherently assume responsibility for pulse detection. Instead, the algorithm operates in a free-running mode, continuously providing pulse arrival time estimates. An external system is responsible for determining when a pulse has arrived and storing the corresponding arrival time estimate at the appropriate moment.

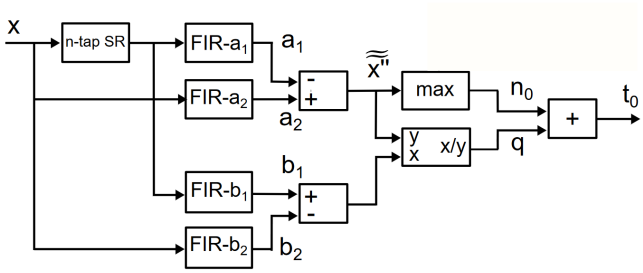

Fig. 13. Schematic diagram of a possible hardware implementation of DLIM.

IX. APPENDIX C: ECAL2 PULSE MODELING

The model presented in Eq. 17 is derived from similar considerations described in [19] and is obtained by modifying an ideal semi-Gaussian pulse shaper $CR\text{-}(RC)^n$ [20], [16], whose pulse shape corresponds to the following equation:

$$f(t) = \alpha \left(\frac{t}{\tau}\right)^n e^{(-t/\tau)} \tag{32}$$

where α and τ are parameters that respectively modulate the pulse amplitude and shape, and n is the number of integrators of the pulse shaper.

This equation assumes an ideal Charge Sensitive Amplifier (CSA), where the output response to a Dirac-delta stimulus, $\delta(t)$, is unrealistically modeled as a step function, leading to an unphysical discontinuity at time $t = 0$.

To more accurately model the onset of the CSA output pulse, we assume an exponential step function with a characteristic time constant τ_r, as follows:

$$CSA(t) = 1 - e^{-\frac{t}{\tau_r}} \tag{33}$$

Considering the new CSA in the pulse model, for $n = 2$, we obtain the following transfer function in the Laplace domain:

$$H(s) = \frac{\alpha\,\tau_d\,\tau_i^2}{(1+s\tau_r)\,(1+s\tau_d)\,(1+s\tau_i)^2} \tag{34}$$

where τ_i, and τ_d are, respectively, the characteristic time constants of the integrators and differentiator of the semi-Gaussian pulse shaper.

If we take the inverse Laplace transformation of Eq. 34 and take the limit when τ_i and τ_d approach τ, and τ_r approaches $\tau/2$, we obtain the following biexponential pulse in the time domain:

$$f(t) = \alpha\, e^{\frac{-2t}{\tau}} \left(-2\tau^2 + e^{\frac{t}{\tau}}\left(t^2 + 2\tau^2 - 2t\tau\right)\right) \tag{35}$$

One last modification must be made to obtain the final model. To separately control the shape by mean of τ, and the amplitude by mean of α, we define a normalization

factor to ensure that the peak amplitude is independent of the exponential time constant τ.

We start by finding the position, $t = t_{max}$, where $f(t)$ is maximum. This corresponds to the value where

$$\begin{cases} \left.\frac{\partial f\,(t)}{\partial t}\right|_{t_{max}} = 0 \\ \\ \left.\frac{\partial^2 f\,(t)}{\partial t^2}\right|_{t_{max}} < 0 \end{cases}$$

which is:

$$t_{max} = 2\left(\tau + \tau\ \mathrm{ProductLog}(e^{-1})\right)$$

By substituting t by this expression of t_{max} into Eq. 35 and making $\alpha = 1$ we obtain the normalization factor F:

$$F = \frac{-2\tau^2 + e^{\frac{2C}{\tau}}(2\tau^2 - 4\tau C + 4C^2)}{e^{\frac{4C}{\tau}}}$$

with C as defined in Eq. 17.

To complete the model, we introduce the term B to describe a constant baseline, and the time of arrival t_0. This gives us the proposed pulse model:

$$f(t) = \begin{cases} B, & t < t_0 \\ B + \alpha e^{-2\frac{t-t_0}{\tau}}\frac{D(t-t_0)}{F}, & t \geq t_0 \end{cases}$$

with $D(t)$ as defined for Eq. 17.

REFERENCES

[1] J. Bortfeldt, F. Brunbauer, C. David, *et al.*, "Precise charged particle timing with the PICOSEC detector," *AIP Conference Proceedings*, vol. 2075, no. 1, p. 080 009, Feb. 26, 2019, ISSN: 0094-243X. DOI: 10.1063/1.5091210.

[2] P. K. F. Grieder, *Exentsive Air Showers and High Energy Phenomena*. Berlin, Heidelberg: Springer, 2010. DOI: 10.1007/978-3-540-76941-5.

[3] D. Belayneh, F. Carminati, A. Farbin, *et al.*, "Calorimetry with deep learning: Particle simulation and reconstruction for collider physics," *The European Physical Journal C*, vol. 80, no. 7, p. 688, Jul. 31, 2020, ISSN: 1434-6052. DOI: 10.1140/epjc/s10052-020-8251-9.

[4] S. Y. Kim, G. B. Ko, S. I. Kwon, and J. S. Lee, "Development of a non-delay line constant fraction discriminator based on the Padé approximant for time-of-flight positron emission tomography scanners," *Journal of Instrumentation*, vol. 10, no. 01, P01005, Jan. 2015, ISSN: 1748-0221. DOI: 10.1088/1748-0221/10/01/P01005.

[5] N. J. Spinks, L. J. Bignell, G. J. Lane, *et al.*, "Pulse Shape Discrimination of low-energy nuclear and electron recoils for improved particle identification in NaI:Tl," *Nuclear Instruments and Methods in Physics Research Section A: Accelerators, Spectrometers, Detectors and Associated Equipment*, vol. 1047, p. 167 773, Feb. 2023, ISSN: 0168-9002. DOI: 10.1016/j.nima.2022.167773.

[6] S. Saxena and A. I. Hawari, "Digital pulse deconvolution with adaptive shaping for real-time high-resolution high-throughput gamma spectroscopy," *Nuclear Instruments and Methods in Physics Research Section A: Accelerators, Spectrometers, Detectors and Associated Equipment*, Symposium on Radiation Measurements and Applications XVII, vol. 954, p. 161 288, Feb. 21, 2020, ISSN: 0168-9002. DOI: 10.1016/j.nima.2018.09.123.

[7] J. Xie, M. Chiu, E. May, Z.-E. Meziani, S. Nelson, and R. Wagner, "MCP-PMT development at Argonne for particle identification," *Journal of Instrumentation*, vol. 15, no. 04, p. C04038, Apr. 2020, ISSN: 1748-0221. DOI: 10.1088/1748-0221/15/04/C04038.

[8] M. Aykac, I. Hong, and S. Cho, "Timing performance comparison of digital methods in positron emission tomography," *Nuclear Instruments and Methods in Physics Research Section A: Accelerators, Spectrometers, Detectors and Associated Equipment*, vol. 623, no. 3, pp. 1070–1081, 2010, ISSN: 0168-9002. DOI: https://doi.org/10.1016/j.nima.2010.08.106.

[9] Y. Fan, L. Zhao, J. Qin, *et al.*, "Research and Verification on Real-Time Interpolated Timing Algorithm Based on Waveform Digitization," *IEEE Transactions on Nuclear Science*, vol. 67, no. 10, pp. 2246–2254, Oct. 2020, ISSN: 1558-1578. DOI: 10.1109/TNS.2020.3022788.

[10] L. Jokhovets, A. Erven, C. Grewing, *et al.*, "Improved Rise Approximation Method for Pulse Arrival Timing," *IEEE Transactions on Nuclear Science*, vol. 66, no. 8, pp. 1942–1951, Aug. 2019, ISSN: 1558-1578. DOI: 10.1109/TNS.2019.2923382.

[11] P. Abbon, E. Albrecht, V. Yu. Alexakhin, *et al.*, "The COMPASS experiment at CERN," *Nuclear Instruments and Methods in Physics Research Section A: Accelerators, Spectrometers, Detectors and Associated Equipment*, vol. 577, no. 3, pp. 455–518, Jul. 11, 2007, ISSN: 0168-9002. DOI: 10.1016/j.nima.2007.03.026.

[12] S. Huber, J. Friedrich, M. Krämer, *et al.*, "Upgrade of the compass calorimetric trigger," *Journal of Instrumentation*, vol. 8, no. 02, p. C02038, Feb. 2013. DOI: 10.1088/1748-0221/8/02/C02038.

[13] P. Abbon, C. Adolph, R. Akhunzyanov, *et al.*, "The COMPASS setup for physics with hadron beams," *Nuclear Instruments and Methods in Physics Research Section A: Accelerators, Spectrometers, Detectors and Associated Equipment*, vol. 779, pp. 69–115, Apr. 11, 2015, ISSN: 0168-9002. DOI: 10.1016/j.nima.2015.01.035.

[14] E. Diekema and T. H. Koornwinder, "Differentiation by integration using orthogonal polynomials, a survey," *Journal of Approximation Theory*, vol. 164, no. 5, pp. 637–667, 2012, ISSN: 0021-9045. DOI: https://doi.org/10.1016/j.jat.2012.01.003. [Online]. Available: https://www.sciencedirect.com/science/article/pii/S0021904512000123.

[15] D.-y. Liu, O. Gibaru, and W. Perruquetti, "Differentiation by integration with jacobi polynomials," *Journal of Computational and Applied Mathematics*, vol. 235, no. 9, pp. 3015–3032, 2011, ISSN: 0377-0427. DOI: https : / / doi . org / 10 . 1016 / j . cam . 2010 . 12 . 023. [Online]. Available: https : / / www . sciencedirect . com / science / article / pii / S0377042710006734.

[16] G. F. Knoll, *Radiation Detection and Measurement*, 4th ed. Hoboken, N.J: John Wiley, 2010, 830 pp., ISBN: 978-0-470-13148-0.

[17] B. Zhang, L. Yang, G. Yan, and X. Zhang, "Comparison of timing discrimination method for pulse-based Lidar," *Infrared Physics & Technology*, vol. 138, p. 105 255, May 1, 2024, ISSN: 1350-4495. DOI: 10.1016/j.infrared.2024.105255.

[18] F. De Dinechin and M. Kumm, *Application-Specific Arithmetic: Computing Just Right for the Reconfigurable Computer and the Dark Silicon Era*. Cham: Springer International Publishing, 2024, ISBN: 978-3-031-42807-4 978-3-031-42808-1. DOI: 10.1007/978-3-031-42808-1.

[19] K. S. Mannatunga, B. Valinoti, W. Florian Samayoa, *et al.*, "Data Analysis and Filter Optimization for Pulse-Amplitude Measurement: A Case Study on High-Resolution X-ray Spectroscopy," *Sensors*, vol. 22, no. 13, p. 4776, Jan. 2022, ISSN: 1424-8220. DOI: 10.3390/s22134776.

[20] W. Sansen and Z. Chang, "Limits of low noise performance of detector readout front ends in cmos technology," *IEEE Transactions on Circuits and Systems*, vol. 37, no. 11, pp. 1375–1382, 1990. DOI: 10.1109/31.62412.